Chapter 3
Topology-Induced Geometry and Properties of Carbon Nanomaterials

Hiroyuki Shima and Jun Onoe

Abstract Nanoscale graphene sheets (i.e., sp^2-bonded monoatomic carbon layers) often exhibit drastic changes in their geometry and properties when non-hexagonal carbon rings are embedded into the original hexagonal lattice. This chapter gives a short review on the physics of sp^2 nanocarbon materials with curved geometry, together with a concise explanation of the mechanism as to how the presence of topological defects causes the anomalously curved geometry. A special emphasis will be placed on the geometry-property correlation inherent in quasi-one-dimensional fullerene polymers and single-walled carbon nanocoils, each of which shows geometric curvature or torsion induced by local change in the carbon network topology.

3.1 Introduction

3.1.1 Carbon as a Building Block

Carbon is one of the most wealth-generating elements on the Earth. In view of biology, carbon is the root of all living matters, allowing many other chemical elements (hydrogen, oxygen, nitrogen, etc.) to react with it to produce substantial organic compounds. From the physico-chemical perspective, carbon is highly versatile in the sense that it accepts different atomic orbital hybridizations. For instance, hybridization of the 2s orbital with all three 2p orbitals (p_x, p_y, and p_z) in a carbon atom results in four sp^3 hybrid orbitals with tetrahedral geometry. The sp^3 orbitals spanning the three-dimensional (3D) space allow the realization of diamond, one of the most

H. Shima
Department of Environmental Sciences, University of Yamanashi, 4-4-37, Takeda, Kofu, Yamanashi 400-8510, Japan
e-mail: hshima@yamanashi.ac.jp

J. Onoe (✉)
Department of Energy Science and Engineering, Nagoya University, Furocho, Chikusa-ku, Nagoya 464-8603, Japan
e-mail: j-onoe@energy.nagoya-u.ac.jp

attractive materials in the world. Similarly, the *s* orbital and two *p* orbitals hybridize to form three sp^2 orbitals with the trigonal planar structure, allowing the formation of graphene, a two-dimensional (2D) mono-atomic sheet made purely from carbon. Finally, the *s* orbital hybridizes with one of the *p* orbitals to form two sp hybridized orbitals, whose frontal lobes face away from each other forming a one-dimensional (1D) straight line.

A direct consequence of the versatility in the hybridized orbitals, each of which spans a different class of spatial dimension (3D, 2D, and 1D), is the diversity of carbon-based nanomaterials with various morphologies [1, 2]. Of the intriguing nanocarbon family, those made by monoatomic carbon layers (i.e., sp^2 graphene sheet) have long been the hot topic in the community of materials science [3]. It is definitely sure that carbon nanotube is the greatest example among the epoch-making nanocarbons made by wrapping a graphene sheet [4, 5]. As well, graphene nanoribbon, which is a stripe of graphene sheet with a few tens Å in width, is also the one spotlighted from the discovery in the last decade [6].

Basically, the profound nature of those sp^2 nanocarbons originates from the perfect hexagonal structure of the monoatomic sheet. And further interesting aspect is that, it may be richer and variegated if the hexagonal symmetry of the crystalline lattice is broken locally by introduction of structural defects [7]. So what kind of symmetry breaking is relevant to the physics of sp^2 carbon? See below an overview of the subject.

3.1.2 Defect in sp^2 Nanocarbon

Ideally, an sp^2 graphene sheet is a perfect 2D crystal in which the carbon atoms perfectly align into hexagons. But in reality, a graphene sheet does not show either perfect horizontality nor perfect hexagonal symmetry. In fact, it inevitably contains a considerable number of defects.

From structural viewpoints, defects in a graphene sheet (or more generally, in a monoatomic layer of sp^2 carbon) are classified into four groups:

(1) Topological defect;
(2) Presence of sp^3 chemical bonds due to hybridization;
(3) Vacancy and/or dislocation;
(4) Non-carbon impurity.

The class of topological defects, written at the top of the list above, is the main topic of this chapter. A topological defect is produced by introducing non-hexagonal rings (e.g., pentagons or heptagons) into the perfect graphene sheet with hexagonal symmetry. We will see later the presence of topological defects may provide a significant alteration in the geometry and properties of sp^2 nanocarbons. Here, the term "topology" means the local connectivity of carbon atoms via covalent bonding, though it has a more abstract meaning as a mathematical jargon [8]. When being inserted in a

graphene sheet, a topological defect breaks locally the structural order of the hexagonal lattice, altering the connectivity of carbon atoms in a limited region. We will see in this chapter that the presence of topological defects can cause a significant alteration in the geometry and properties of the originally planar sp^2 nanocarbon sheets.

Emphasis should be placed on the fact that the defect-induced alteration in geometry can allow a new class of anomalously-shaped nanocarbon materials endowed with surface curvature and/or torsion. Examples include, but are not restricted to, peanut-shaped fullerene polymers [9], helix-shaped carbon nanocoils [10], and gyroid-shaped carbon Schwarzite [11]. Many intriguing properties of the three anomalously-shaped nanocarbons have been unveiled in the last decade. Against the backdrop, the present chapter aims at a bird's eye view of the latest achievements on the new family of sp^2 nanocarbon materials, together with a concise explanation as to how the topology of local atomic structure correlates with global geometry of the sp^2 nanocarbon materials.

3.2   Topology-Induced Geometry in sp^2 Nanocarbon

3.2.1   Surface Curvature Generation in Graphene Sheets

Topological defects play a crucial role in tailoring equilibrium structures of graphene sheets [12, 13]. This is because insertion of topological defects into a graphene sheet causes a change in local connectivity of carbon atoms, resulting in a global change in the geometry of the sheet from the planar to curved structure as explained below.

Figure 3.1 provides a schematic diagram of surface curvature generation by topological defect insertion [14, 15]. Suppose that we are given a monoatomic graphene sheet with perfect hexagonal symmetry, as displayed in the middle panel of Fig. 3.1. Next, we remove a $\pi/3$ wedge from the original sheet and pull the two new edges to connect them with each other. The resulting structure is displayed in the left panel of Fig. 3.1. A particular attention should be paid to that the local atomic connectivity is altered only at the central carbon rings, from hexagon to pentagon, while other hexagon rings surrounding the central non-hexagon ring remain unchanged. This diagram thus shows that artificial insertion of a pentagon ring into the perfect hexagonal sheet yields a transformation from the flat to a positively curved graphitic layer.

A contrasting situation is illustrated in the right panel of Fig. 3.1. In that situation, one $\pi/3$ wedge hatched in the middle panel is replaced forcibly by an already-joined two $\pi/3$ wedges. As a consequence, the originally flat sheet (middle panel) is transformed to a saddle-shaped graphitic sheet that has a heptagonal ring at the center (right panel). Similarly to the previous case, local atomic configuration remains unchanged except for the central non-hexagonal ring.

We have known that artificial change in the local atomic connectivity at the center of a planar graphitic sheet results in a positively or negatively curved graphitic
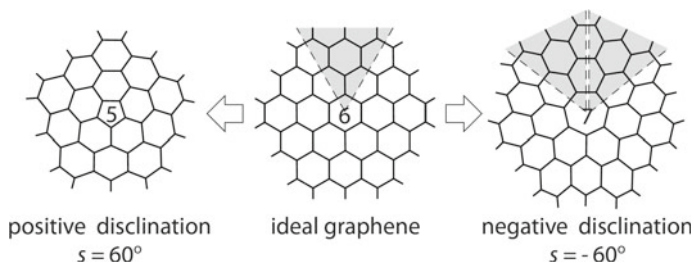
Fig. 3.1 Diagram of surface curvature generation by topological defect insertion. A portion of an initially flat graphene sheet (middle) becomes endowed with positive (left) or negative (right) surface curvature when a $\pi/3$ wedge (shaded area) of the original sheet is removed or added, respectively. Reprinted with permission from [15]

Fig. 3.2 A wrinkled graphene structure. It was theoretically designed through a controlled distribution of topological defects. Reprinted with permission from [17]
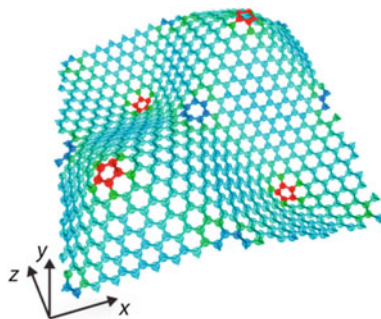
sheet. So what happens if the central hexagon is replaced by larger rings (e.g., octagon, nonagon, or more) or smaller rings (square and triangle)? In principle, a severely curved sheet with positive or negative surface curvature can be built through such local connectivity alteration; however, most of them turned out to be unstable mechanically and thus it will be difficult to synthesize them in reality [16].

The topology-induced change in the surface geometry implies the ability of morphological control of sp^2 nanocarbons by artificial insertion of topological defects. In fact, numerical simulations have suggested that collective behaviors of topological defects can be utilized to design wrinkled graphene structures in controllable manner. Figure 3.2 shows a thermodynamically stable structure of a defective graphene sheet obtained by molecular dynamics simulations [17]. The numerically obtained structure shows concavo-convex shape, involving pentagons at crests and valleys and heptagons at saddle points. The simulation revealed the mechanical stability of the periodically curved structure with 4 nm in wavelength and 0.75 nm in amplitude.

It was theoretically predicted that the topology-induced curvature in a graphene sheet leads to a significant modification of the physical properties [18] such as electronic band structure [19–21], the charge carrier transport [22, 23], and spin-orbit couplings [24]. In particular, negatively curved graphene sheets embedding heptagonal and octagonal defects have been shown to significantly enhance the capacity
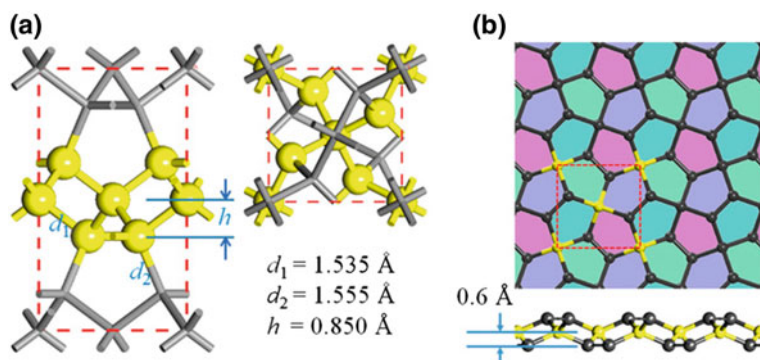
Fig. 3.3 **a** Three-dimensional crystal structure of T12-carbon, from which the two-dimensional pentagon-based sheet (highlighted in yellow) will be exfoliated. Views from the [100] and [001] directions are displayed. **b** Two-dimensional all-pentagon-made monoatomic carbon sheet, called "penta-graphene". Top and side views are shown. Reprinted with permission from [27]

of graphene based electrodes [25, 26], because of the high surface area compared with the planar counterpart. More recently, another graphene sheet consisting of only pentagons (so called "penta-graphene") has been proposed theoretically as shown in Fig. 3.3 [27]. It is interesting to note that penta-graphene exhibits a negative Poisson ratio.

3.2.2 Plastic Deformation of Carbon Nanotubes

Aside from the "planar" graphitic materials, artificial introduction of topological defects into "tubular" sp^2 nanocarbons is also an interesting subject; defect insertion can cause drastic changes in the structure and property of the tubular systems. For instance, X-branched and T-branched junctions made of carbon nanotubes were synthesized by inserting topological defects into the joint area of two or more different nanotubes, as demonstrated in Fig. 3.4 [28–30]. These branched nanocarbons will find useful applications in nanoelectronics [31] and fiber-reinforced composites [32, 33]. Other interesting examples of anomalously shaped nanotubes include carbon nanocoils [34] and bamboo-shaped carbon nanotubes [35–37]. The structural anomaly observed in these systems relies on the periodic insertion of defects into the originally straight nanotubes, which causes periodic variation in torsion and/or curvature that allow coiled and/or twisted structures as metastable states.

Figure 3.5 demonstrates spatial variation in the tube radius caused by topological defect insertion into a carbon nanotube [38, 39]. The symbol "P" depicted in the electron microscope image indicates an apex at which one pentagon is embedded into a graphitic cylinder. The presence of the pentagon causes mechanical strain in the hexagonal carbon network around the pentagon. To relieve the strain, the cross-
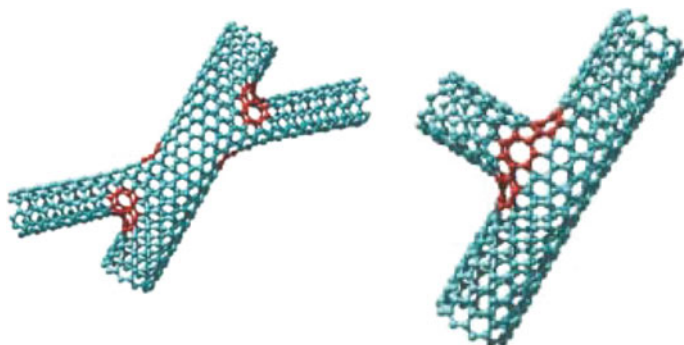
Fig. 3.4 Left: Molecular models of the X-junction between a thin and wide nanotube. Heptagonal rings are indicated in red. Right: Atomic models of the T-junction. Reprinted with permission from [28]

section of the tube slightly deviates from the initial circular shape at the position indicated by "P", resulting in an oval shape. Another strain-induced deformation occurs at a local dent, indicated by "H" in the microscope image of Fig. 3.5. At the dent, one heptagon is embedded into the graphitic sheet, generating negative surface curvature near the point. As a result of the paired defects, a pentagon and a heptagon, the tubular diameter of the carbon nanotube decreases gradually from the trunk to the tip of the nanotube.

Interestingly, topological defects in carbon nanotubes (and other nanocarbons having a closed shape) shed light on a beautiful interplay between mathematics and atomic structures. A typical example is a capped structure of a nanotube obtained by defect insertion [40]. Figure 3.6 shows an enlarged view of the tip of a capped carbon nanotube with chirality of (30,0). Two different capped structures, shown in the panels (a) and (b), are obtained by inserting six pentagon defects at the tip. An intriguing fact is that the axial symmetry of the resulting capped structure is dependent on the relative configuration of the topological defects, even if the same number of defects is inserted. Indeed in Fig. 3.6, the exactly six pentagonal defects yield five-fold symmetry in the case of (a) and six-fold symmetry in (b) with respect to the tubular axis, in which more surprisingly, it is prohibited to choose the other number of pentagons to be embedded; only the six pentagon insertion is allowed for capping a carbon nanotube regardless of its tube radius and chirality. This restriction with respect to the number of pentagons is a consequence of a mathematical theorem, called the Gauss-Bonnet theorem [41]. The theorem states that the number of non-hexagonal rings (i.e., topology) is related to the curvature of the embedding graphene sheet (i.e., geometry). From the technological perspective, the closed-cap formation driven by topological defect insertion has been expected to offer the possibility for the control of the chirality of carbon nanotubes during growth [42].
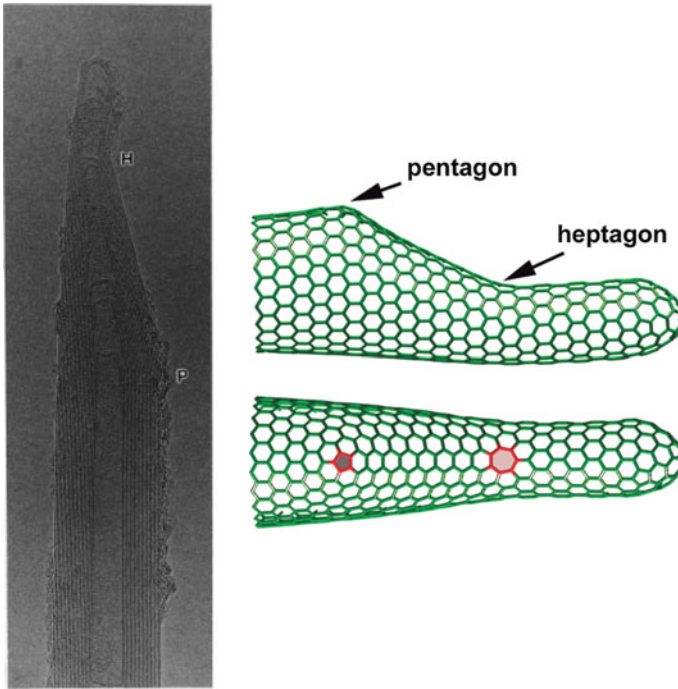
Fig. 3.5 Left: Electron microscope image of a closed cap at the tip of a multi-walled carbon nanotube. The successive presence of topological defects changes the diameter of the concentric tubes gradually toward the tip [38]. Right: Atomistic structure of a capped carbon nanotube, in which one pentagon and one heptagon are incorporated. The overall picture looks similar to the image shown in the left panel. Reprinted with permission from [39]

3.3 Stone-Wales Defect

3.3.1 Symmetry Breaking by C–C Bond Rotation

A Stone-Wales (SW) defect, or also called a 5-7-7-5 defect, is the lowest energy topological defect in sp^2 nanocarbons [43]. It is formed by a 90-degree rotation of a C–C bond in the hexagonal carbon network. The rotation causes atomic re-configuration at the neighbor from the set of four hexagons to the set of two pentagons and two heptagons; see the top panels in Fig. 3.7. This 90-degree bond rotation is often called a Stone-Wales (SW) transformation. It should be noted that the bond rotation breaks the hexagonal symmetry of the perfect graphene sheet. Thus the resulting SW defects scatter carrier transport, degrading the high mobility of carriers, which is the hallmark of Dirac fermion behavior in graphene [44]. Yet it is not always a bad thing. In fact, the symmetry breaking induced by SW defect insertion is also manifested by
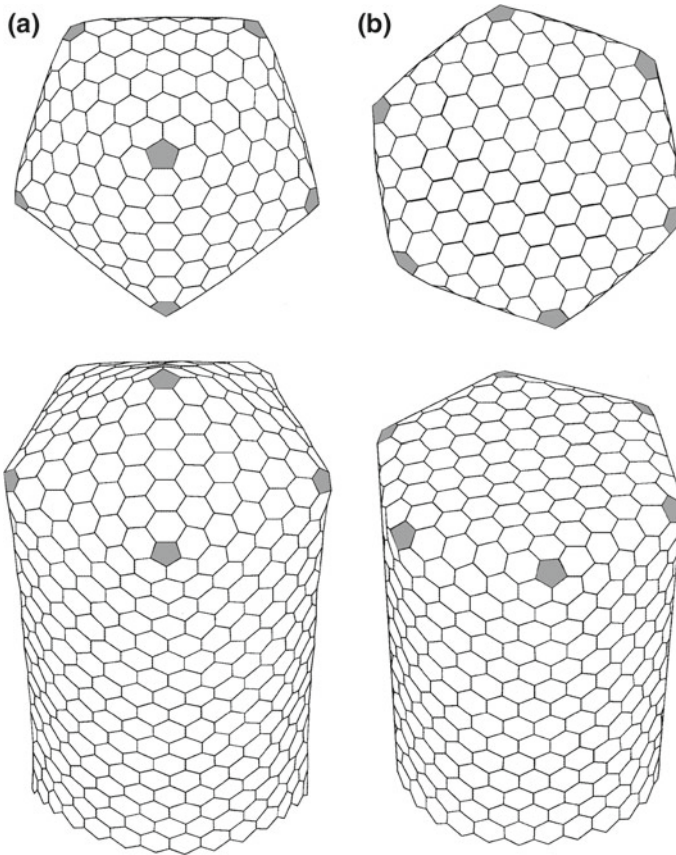
Fig. 3.6 Capping a (30,0) zigzag carbon nanotube by inserting six pentagonal carbon rings (marked by shadow) at the tip. Depending on the defect configuration, two different kinds of axial symmetry arise in the capped structure: **a** five-fold and **b** six-fold symmetry. Top views and overall views are displayed in the upper and bottom panels, respectively. Reprinted with permission from [40]

the band gap opening in the electronic spectrum of graphene [45]. This finding will expand the range of possible applications of graphene in nanoelectronics.

3.3.2   Formation Energy

Let us remind that SW transformation is accompanied by the consecutive breaking of two single C–C bonds. Since the breaking of a single C–C bond in graphene requires expending energy of nearly 5 eV, the height of the potential barrier preventing the SW transformation is on the order of a few eV or more [46]. If we choose thermal activation to overcome the high-energy barrier, it would be necessary to use extremely
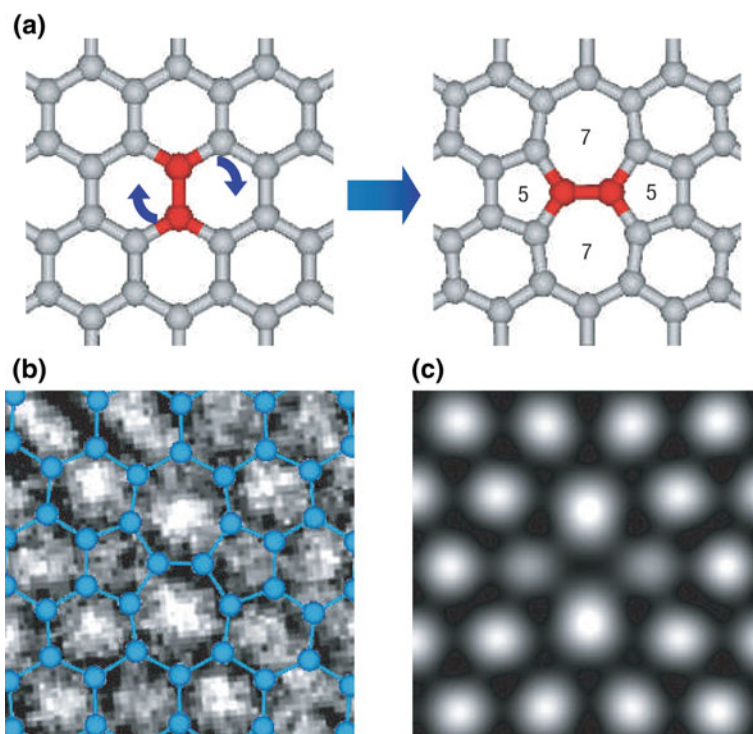
Fig. 3.7 Top: Atomic configuration of a graphene sheet before (left) and after (right) rotating the C–C bond marked in red. Bottom left: Electron microscopic images of a SW defect. Bottom right: Simulated results of the atomic configuration obtained by density functional theory. Reprinted with permission from [53]

high temperatures. Therefore, earlier experimental attempts at artificial production of SW defects have been based on the high-energy beam irradiation or the action of mechanical stresses at the stage of the synthesis of the sp^2 nanocarbons, as will be argued in Sect. 3.4.

3.3.3 Out-of-Plane Displacement

One may think that a graphene sheet is flat and purely two-dimensional, even when a SW defect is present in the sheet. But this is not true; in fact, the lowest-energy atomic configuration of the SW defect has a sine-wave-like form [47]. In this wavy structure, the two atoms involved in the rotated C–C bond move out of plane in the opposite direction. This buckling of the C–C bond at the core of the SW defect gives rise to the vertical displacement of many atoms around the defect, resulting in a sine-like shape of the cross section as illustrated in Fig. 3.8 [47].
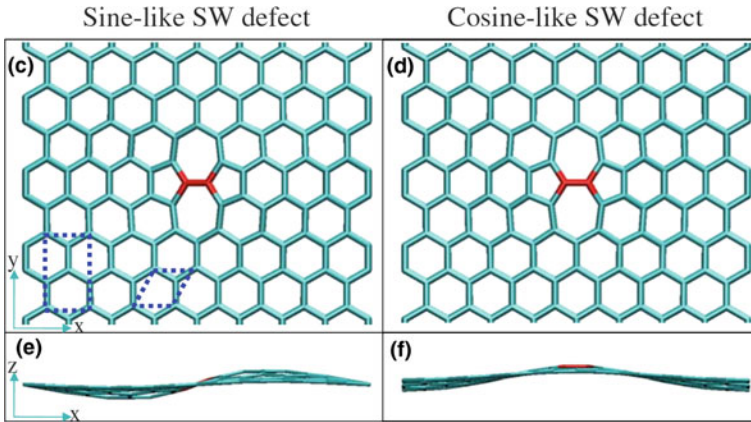
Fig. 3.8 The structure of two buckled SW defects in graphene. Left: Top and side views of the sine-like buckled SW defect, being identified as the most stable defect structure. Right: Top and side views of the cosine like buckled SW defect. The rotated bonds at the defect core are highlighted. Dashed lines indicate 1×1 rectangular and hexagonal unit cells. Reprinted with permission from [47]

It may be non-trivial for readers why the SW defect in graphene does not remain flat in equilibrium but buckles out of the plane. One plausible mechanism is based on the release of the excess strain energy induced by the C–C bond rotation [47]. Prior to the bond rotation, the equilibrium C–C bond length in perfect graphene is 1.42 Å. If we rotated a C–C bond with keeping the original flat shape of the embedding hexagonal sheet, the separation between the rotated atoms would be compressed to 1.32 Å. Here, the flat structure cannot release the compression efficiently, because in-plane motion of C atoms in graphene is too much expensive as compared to out-of-plane motion. Instead of the in-plane deformation, the SW defect exhibits out-of-plane deformation, as a result of which the compressed C–C bonds can be expanded enough to release the in-plain strain energy. In fact, displacement of the SW defect in the direction normal to the graphene sheet results in the pulling of neighboring atoms out of the plane, because it is energetically favorable for the C–C bonds that surround the SW defect to remain as close to a planar sp^2-bonded network as possible.

SW defects also affect the side-wall curvature of carbon nanotubes. Figure 3.9 illustrates local deformation of a nanotube caused by SW defect insertion into the graphitic sidewall [48]. It follows from Fig. 3.9 that the magnitude of out-of-plane displacement is maximized at the interface between two pentagons. Because of the significant out-of-plane displacement, addition reactions are most favored at the C–C double bonds of these positions [49].
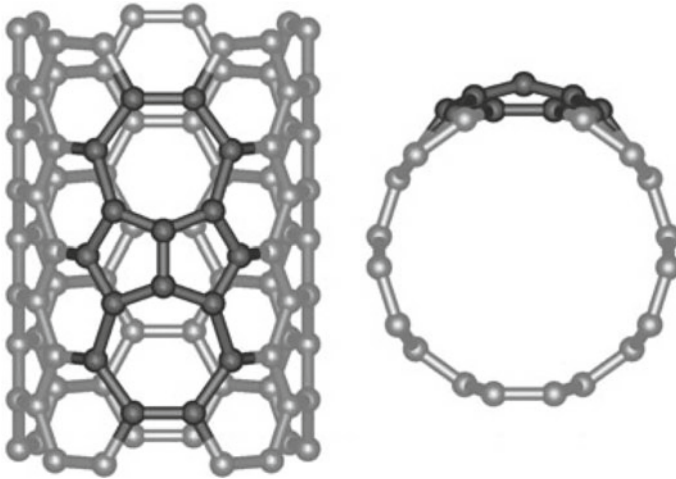
Fig. 3.9 Stone-Wales defect on the sidewall of a single-walled carbon nanotube. Reprinted with permission from [48]

3.3.4 Microscopic Observation

From an experimental viewpoint, it is difficult to observe SW defects by ordinary microscope techniques, despite a few indirect evidences have been provided to date [50–52]. The difficulty stems mainly from the high activation barrier for the SW transformation, whose energy scale is estimated as a few eV [30]. Due to the high activation barrier, detection of native topological defects in a pristine sp^2 nanocarbon is statistically unrealistic. Hence most of earlier experiments for identifying topological defects with an atomistic-scale precision were based on artificial generation of the defects, with the aid of high-energy beam irradiation and/or high-temperature heat treatment.

The first direct observation of SW defects was successful on single-walled carbon nanotubes in 2007 [53]. In the seminal work, high-resolution transmission electron microscopy with atomic accuracy was used to obtain the image that is displayed in the left-bottom panel of Fig. 3.6. It is interesting to remind that the defects shown in the image were those artificially introduced in a pristine non-defective carbon nanotube. Being exposed to high temperature (≈2300 K) in vacuum, a portion of hexagonal lattices at the sidewall of nanotubes breaks out, which leads to the fusion of adjacent nanotubes into a unified single-walled nanotube with large tube diameter [54]. The large-diameter nanotube thus obtained suffers from substantial amount of structural imperfection. When rapidly cooled, therefore, a large number of SW defects as well as other kinds of topological defects are involved in the resulting nanotube; typically a few SW defects can be detected per 10 nm length (and/or per 10 nm long).

Aside from those found in carbon nanotubes, SW defects were also found in a flat monolayer graphene [55]. Figure 3.10 shows the microscope image of SW
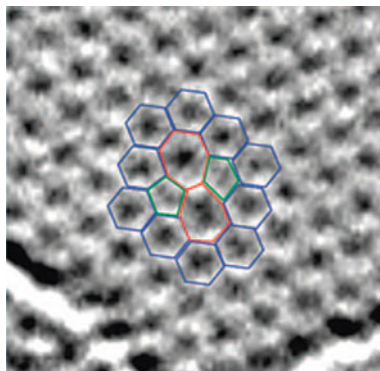
defects involved in the two-dimensional graphitic sheet; pentagons and heptagons
are colored in green and red, respectively. The image provides clear evidence for SW
defects existing in the examined graphene layer.

Quite recently, statistical atomic kinetics during SW transformation in graphene
was formulated, enabling the decoupling of the two contributions from high-energy
beam irradiation and thermal excitation to the activation of the C–C bond rotation
[56]. The result indicated the exceptionally high rate of healing for SW defects
generated by irradiation, compared with the healing rate of thermally-induced SW
defects. This implies the complexity in the route of reaction processes toward SW
defect realization in a graphene sheet.

3.4 Defect of 5–7 Paired Type

3.4.1 Dissociation of a SW Defect

It is interesting to note that SW defects on the sidewall of carbon nanotubes can
show a curious mechanical response to the axial load. Upon application of the axial
load to the defective carbon nanotube, a SW defect can dissociate into two separated
5–7 pairs. This tensile-driven dissociation of a SW defect is caused by additional
transformations of C–C bonds that locate in the vicinity of the 5–7 pairs [57]. Now
we suppose that the axial load remains exerting continuously on the nanotube. Then
we will observe further successive transformations of C–C bonds around the 5–7
pairs. Because of the successive transformations, the 5–7 pairs start to migrate along
a helical path that twines around the tube [58].

The migration of the 5–7 pairs along the helical path involves a number of atomic
reconfigurations around it, thus requiring a sufficient amount of energy supply to
proceed. This requisite energy is often supplied in the form of thermal excitation and
the work done by axial strain; it can be also supplied by bend deformation [59, 60].
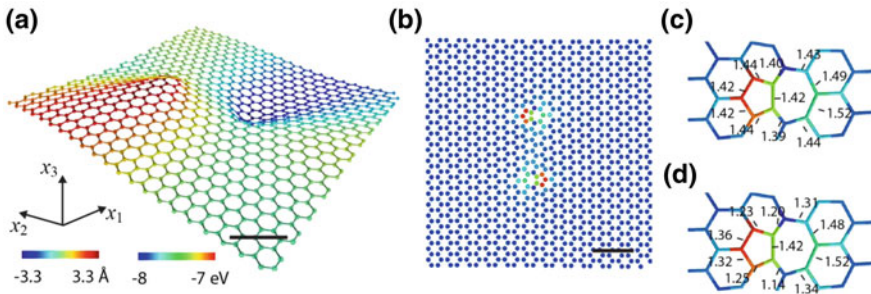
Fig. 3.11 **a**, **b** A perspective view (**a**) and a top view (**b**) of the atomic configuration involving two 5–7 paired defects in a graphene sheet. **c**, **d** Bond structures around the defect core in 3D (**c**) and 2D projection (**d**). The color represents the scale of the out-of-plane displacement in **a** and potential energy in **b**–**d**, respectively (scalebar: 1 nm). Reprinted with permission from [61]

The chirality alteration is an important consequence of the 5–7 pair migration. When the 5–7 pairs complete the full distance from one end to the other end of the given nanotube, the charity of the tube domain covered by the helical path will be altered. This chirality change is accompanied by the change in the tube diameter. Therefore, the defect migration may serve as a driving force for a ductile elongation behavior of carbon nanotubes under large axial strain, as was observed in experiments [57].

3.4.2 As a Seed of Surface Curvature

We have seen in Sect. 3.3 that the presence of SW defects causes a surface curvature in an originally flat graphene sheet. Similar curvature generation occurs in a graphene sheet containing topological defects of an isolated 5–7 pair, i.e., an adjacent pair of pentagonal and heptagonal rings. Figure 3.11 illustrates the wrinkle of an initially flat graphene produced by inserting two 5–7 defects [61]. As shown in the middle panel, the two 5–7 defects are placed apart from each other with a separation equivalent to several hexagonal rings. Then the two defects generate the surface curvature, giving rise to a large wrinkle near the defect core (see the left panel). The vertical amplitude of the out-of-plane displacement is estimated to be up to 3.3 Å. The middle panel of Fig. 3.11 shows the potential energy of carbon atoms around a 5–7 defect, where atoms involved in the defect exhibit a higher energy than those far from the defect. In particular, three atoms on the heptagon side have the highest energy. The right two panels display the 3D distributions of bond lengths around a defect (top) and the corresponding 2D projection (bottom). It can be clearly observed that the 2D projection significantly underestimates the length of covalent bonds around the 5–7 defect.

Fig. 3.12 Schematic illustration showing the synthesis of the 1D C_{60} polymer. Reprinted with permission from [65]
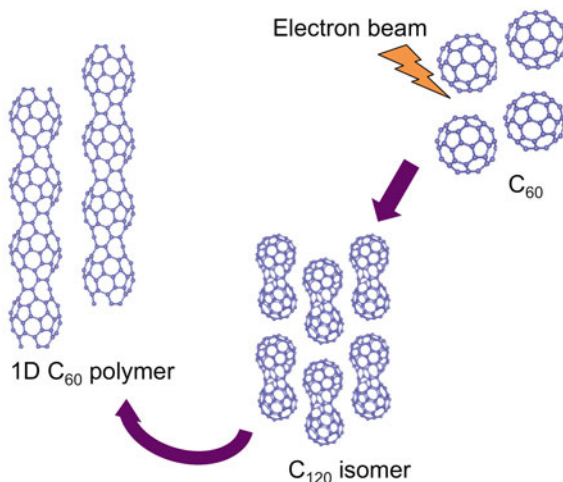
3.5 Peanut-Shaped C_{60} Polymers

3.5.1 Fusion of C_{60} Molecules

In the previous sections, we have seen that alteration in local atomic configuration of sp^2 nanocarbons can lead to a drastic change in the global geometry. Artificial control of topology in the carbon sheet, therefore, may enable to realize anomalously shaped sp^2 nanomaterials endowed with surface curvature. This section focuses on a particular class of such anomalously shaped sp^2 nanocarbons, called peanut-shaped fullerene (C_{60}) polymer [9]. It is a quasi-one dimensional (1D) nanostructure obtained by a series of fusions between C_{60} molecules [62, 63]. Figure 3.12 shows a schematic diagram of the synthesis. When irradiated by the high-energy electron beam, two C_{60} are coalesced with each other via the generalized SW transformation [64]. They are then transformed into C_{120} isomers, followed by the synthesis of the 1D C_{60} polymer [65].

It has been unveiled that the 1D C_{60} polymer exhibits unique properties differing from those of the other nanocarbon allotropes (fullerenes, nanotubes, and graphenes) [66]. Experimental findings on the Peierls transition [67] and the infrared (IR) absorption intensity [68, 69] have indeed suggested the intriguing correlation between the shape and physical properties of the 1D C_{60} polymers. The most interesting properties in view of topology-geometry correlation would be the surface curvature effects on the electronic properties. Indeed, the 1D C_{60} polymers commonly show the periodic modulation in the surface curvature of the sidewall along the tubular axis. This curvature modulation stems from periodic variation in the tube diameter, which results from periodic insertion of topological defects into a rolled-up graphene sheet. We will see in the subsequent sections that the periodically modulating curvature of the

1D C_{60} polymers drastically changes the nature of collective excitations in the mobile electrons compared with the case of the flat sp^2 nanocarbons.

3.5.2 TLL State in C_{60} Polymers

The 1D C_{60} polymer is a long, thin, and hollow cylinder whose radius varies periodically in the axial direction. Generally, in low-dimensional systems, Coulombic interaction between mobile electrons plays a crucial role in their quantum nature and often creates new collective states. Particularly in one-dimensional systems, such as the 1D C_{60} polymer, interacting electrons cannot be regarded as a Fermi-liquid but as a Tomonaga-Luttinger liquid (TLL) [70]. In the TLL state, the single-particle excitation spectrum has an energy gap near the Fermi level, and this gap often causes a power-law anomaly in the measurement data of the system. The hallmark of TLL states is the power law behavior of the single-particle density of states (DOS), designated by $D(\omega, T)$, near the Fermi energy E_F. Here, ω indicates the energy measured from E_F, and T denotes the absolute temperature. Such power-law anomalies were experimentally confirmed in carbon nanotubes [71], which are also a quasi-one dimensional nanocarbon. These facts naturally raise a question as to whether or not the periodic curvature modulation inherent to the 1D C_{60} polymers affects the TLL behavior of the systems if it occurs [72]. Given a significant effect is detected, it evidences the topology-induced alteration both in the geometry and property of the 1D C_{60} polymers.

The mentioned above problem was resolved experimentally in 2012 by photoemission spectral (PES) measurements [73]. The measurements revealed the PES spectra in the vicinity of E_F in the temperature range of 30–350 K. As the temperature decreased, the DOS $D(\omega, T)$ converged to a power-law whose dependence on the binding energy ω near E_F is described by

$$D(\omega, T = 0) \propto |\hbar\omega - E_F|^{\alpha}$$

in an energy range of 18–70 meV with the exponent α of ca. 0.66. In a similar manner, the DOS just on E_F (i.e., $\omega = 0$) was found to obey the power law with respect to T as

$$D(\omega = 0, T) \propto T^{\alpha}$$

in the range of 30–350 K with α being ca. 0.59. It should be emphasized that the above mentioned values of α, nearly equal to 0.6, are quite larger than that of single-walled carbon nanotubes ($\alpha \sim 0.5$) [71]. It is thus concluded that the feasible increment in α obtained in the experiment can be attributed to the effect of surface curvature modulation that are produced by the periodically inserted topological defects along the tube axis.
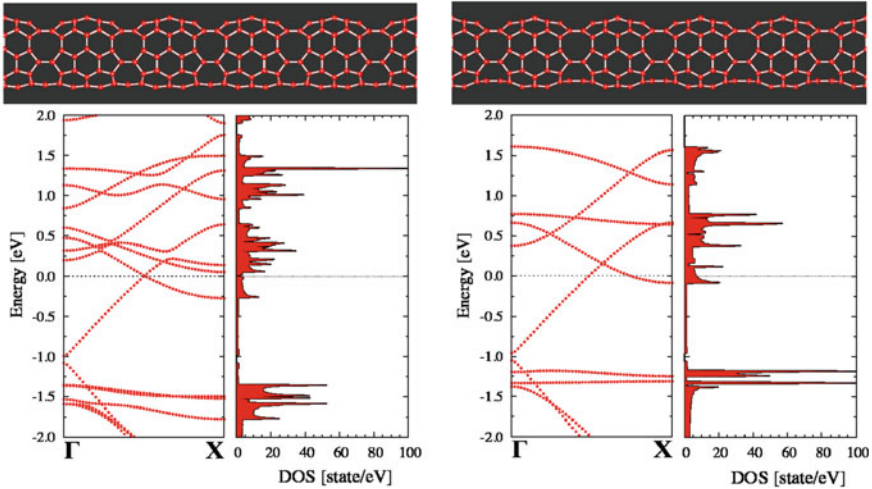
Fig. 3.13 Top: Two different atomic models of the 1D C_{60} polymers deduced from first-principles calculations. Constricted portions are occupied by a set of heptagons and octagons in the left-side model, and by a set of five octagons in the right-side model. Bottom: Dispersion curves and the densities of states of electrons in the two atomistic systems. Reprinted with permission from [72]

3.5.3 Topology-Based Understanding

Theoretical interpretation regarding the TLL behavior of the 1D C_{60} polymer has been proposed in 2016 [72], shortly after the experimental finding reported in 2012 [73]. The aim of the theoretical work was to describe the low energy behavior of local DOS in the 1D C_{60} polymer using the bosonization procedure. This procedure requires the knowledge above the Fermi velocity of carriers, which can be evaluated from the electronic band structures. To secure the quantitative accuracy, the band structures as well as the atomic configuration of the 1D C_{60} polymers were deduced from the first-principles calculations [74], from which the correlation between topological defects and the TLL nature can be unveiled.

Figure 3.13 shows the energetically stable atomic models of the 1D C_{60} polymers deduced from the first-principles calculations [74]. To find the two most stable configurations, more than fifty kinds of 1D C_{60} polymers having different atomic structures were analyzed. Through the analysis, it turned out that the total energy and the stability of the models depend on the number of non-hexagonal rings (i.e., pentagon, heptagon, and octagon) embedded and their relative positions. One of the two most stable models, depicted in the left-upper panel of Fig. 3.13, is characterized by that the constricted portions are occupied by a set of heptagons and octagons. On the other hand, the constricted parts of the other stable model depicted in the right-upper panel are composed of five octagons. The difference in the formation energy between the two models was found to be less than 0.7 eV; in actual fabrication of the 1D C_{60} polymers, therefore, both atomic configurations are possibly realized.

The bottom panels of Fig. 3.13 show the electronic energy bands of the two models. It follows from the graphs that more than one dispersion curves cross the Fermi level. A difference in the number of Fermi-level crossing points between the two models is a consequence of the slight difference in the lattice symmetry at the waist part as mentioned above. Another remarkable feature is that for both models, the X-shaped band crossing is a little slanted, asymmetric at the crossing point. This slanted level crossing is in contrast with the fully symmetric level-crossing observed in the metallic single-walled carbon nanotubes, indicating the effect of periodic insertion of topological defects in the rolled-up sp^2 monoatomic sheet.

The simulation data for the stable lattice structure and the associated electronic band structure made it possible to obtain an analytic formula for DOS of the 1D C_{60} polymers. The formula successfully reproduces the experimental data of PES, thus describing the effect of topological defects on the TLL nature. Furthermore, the formula tells us that different Fermi-level-crossing bands result in different power-law dependence in the PES. This conclusion implies an uncovered crossover in the spectra at energy on the order of 100 meV, beyond which the value of the exponent shifts significantly.

3.5.4 Curvature-Based Understanding

We have argued in Sect. 5.3 that the atomistic model involving topological defects provides the theoretical understanding of the TLL states realized in the 1D C_{60} polymers. Periodic insertion of defects causes variation in the surface curvature of the sp^2 monoatomic sheet, resulting in the upward shift in the power-law exponent compared with that of single-walled carbon nanotubes.

The story does not end. If the wavefunctions of the mobile electrons are expanded over the whole system, as those in 1D C_{60} polymers [75], there is another theoretical approach that is useful to describe the low-energy excitations of the electrons moving on curved surfaces. In this approach, the discrete atomic structure is approximated as a continuum thin surface, and the electrons' motions are assumed to be restricted to the surface by a confining force perpendicular to the surface [76]. Due to the strong confinement, quantum excitation energies in the direction normal to the surface are elevated much higher than those in the tangential direction. As a result, the particle motion normal to the surface can be disregarded; this approximation allows us to define an effective Hamiltonian for propagation along the curved surface.

It is well known that, given a curved surface, the effective Hamiltonian describing the quantum motion on the surface involves an effective scalar potential. The sign and magnitude of the effective potential depend on the local surface curvature. An important consequence derived from the effective potential term in the Hamiltonian is that quantum particles confined to a thin curved layer should behave differently from those on a flat plane. Namely, the presence of nonzero surface curvature impacts the quantum motion of electrons in the curved system. In this context, it is expected
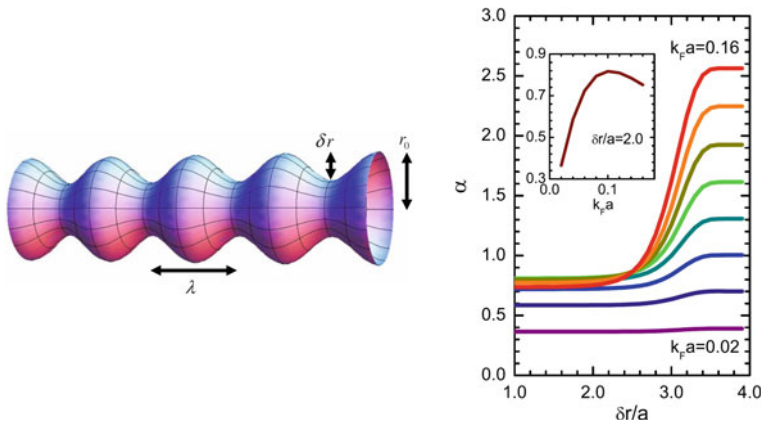
Fig. 3.14 Left: Schematic illustration of a quantum hollow cylinder with periodic radius modulation. Right: Surface curvature effect on the TLL power-law exponent. Reprinted with permission from [77]

that the periodic surface curvature inherent in the 1D C_{60} polymers engenders sizable effects on their TLL properties.

The problem was addressed theoretically in 2009 using the continuum approximation [77]. There, the 1D C_{60} polymers were mapped onto thin, long, and hollow cylinders; the cylindrical radius is assumed to be varied in a periodic manner, as analogous to the envelope surface of the real C_{60} polymers. The tube radius $r(z)$ was assumed to be periodically modulated in the axial z direction as

$$r(z) = r_0 - \frac{\delta r}{2} + \frac{\delta r}{2} \cos\left(\frac{2\pi}{\Lambda} z\right)$$

where the parameter r_0 and δr were introduced to express the maximum and minimum of $r(z)$ as r_0 and $r_0 - \delta r$, respectively; see Fig. 3.14 for the schematic illustration of the deformed tube. The values of the parameters, $r_0 = 4.0$ Å and $\Lambda = 8.0$ Å, suffice to reproduce the actual shape of the 1D C_{60} polymers, while the value of δr may vary according to the time duration of electron beam irradiation applied to pristine C_{60} molecules at the stage of synthesis. It is important to note that the value of δr determines the degree of curvature-induced scalar potential. Therefore, the central aim is to be placed on where (or not) the variation in δr causes a certain shift in the TLL power-law exponent α.

Let us remind that given a TLL state, the single-particle DOS at zero temperature, $D(\omega)$, near E_F exhibits a power-law singularity of the following form:

$$D(\omega) \propto |\hbar\omega - E_F|^\alpha, \quad \alpha = \frac{u + u^{-1}}{2} - 1$$

The explicit form of u is derived using the bosonization procedure as follows:

$$u = \sqrt{\frac{2\pi \hbar v_F + g_4\left(q\right) - g_2\left(q\right)}{2\pi \hbar v_F + g_4\left(q\right) + g_2\left(q\right)}}$$

Here, $g_4\left(q\right)$ and $g_2\left(q\right)$ are the wavenumber(q)-dependent coupling constants, and v_F is the Fermi velocity, determined by the slope of the electronic dispersion curve at the Fermi level. Note that the variation in δr causes a change in the dispersion curve; thus v_F is a function of δr. As a consequence, the exponent α should be dependent on δr, as clearly observed in Fig. 3.14. The plot shows the numerical result of the δr-dependent α for different Fermi wavenumber k_F. The salient feature of Fig. 3.14 is the significant increase in α with increasing δr. Such surface curvature-driven shift in α is consistent with the experimental finding that α for the 1D C_{60} polymers is larger than that for straight-shaped carbon nanotubes. Eventually, the upward shift in α can be attributed to the effects of geometric curvature as well as topological defect insertion to the constituent sp^2 monoatomic sheet

3.5.5 Electron-Phonon Coupling in C_{60} Polymers

It is plausible that topological defect insertion, or equivalently, periodic modulation in surface curvature, may affect the degree of electron-phonon (e-ph) interaction in the 1D C_{60} polymers. This is because the spatial profiles both of lattice vibration amplitude and the probability density of electron's wavefunctions will be dependent on the atomistic-level topology and global geometry of the system. In general nanocarbon allotropes, the e-ph interaction plays the key role in the collective motion of carriers, as proved in superconductivity [78] and charge density waves (CDW) [79]. Thus the theoretical prediction as well as experimental detection of the strength of e-ph interaction in the 1D C_{60} polymers will facilitate the understanding of their physico-chemical properties and of the contribution from the topological effects on them.

To proceed with consideration, we remind that in sp^2 nanocarbons, the strength of e-ph coupling is highly dependent on the global geometry of the structures. Denoting the e-ph coupling strength by λ, it is known that $\lambda \sim 0.6$ for K_3C_{60} having spherical structure [80], $\lambda \sim 0.006$ for single-walled carbon nanotubes having monolayered tubular structure [81] and $\lambda \sim 5.4 \times 10^{-4}$ for multi-walled nanotubes having concentric-layered cylindrical structure [82]. The wide variation in the values of λ, despite the common sp^2 nature, is plausibly attributed to the difference in the morphology of extended π-conjugation in the system. So what value of λ should be obtained for the 1D C_{60} polymers, having an intermediate geometry between the "spherical" C_{60} molecules and the "tubular" carbon nanotubes?

In order to estimate λ, carrier relaxation dynamics of the 1D C_{60} polymers was examined using femtosecond time-resolved pump-probe spectroscopy [83]. The measurement data of the femtosecond-transient refractivity was theoretically analyzed, leading to the conclusion that the magnitude of λ of the 1D C_{60} polymers to

be 0.02. This result indicated that topology-induced curvature in the sp^2 nanocarbons significantly affects the magnitude of λ for nanocarbon allotropes.

3.6 Carbon Nanocoil

3.6.1 Benefit from Coiled Structure

Topological defect insertion into sp^2 nanocarbon allows to realize not only "curved" structures but also geometrically "twisted" ones. Carbon nanocoil is a typical example of such twisted sp^2 nanocarbon, resembling a "telephone cord" attached to a traditional phone receiver [84]. Carbon nanocoil promises to show both mechanical flexibility reflecting the coil morphology and the mechanical toughness originating from the sp^2 bonding. Furthermore, unique spiral structures of carbon nanocoils imply their versatile applications [85] including ultra-sensitive contact with resolution as high as femtograms [86].

From a historical perspective, the existence of carbon nanocoils was theoretically predicted in advance of the experimental realization. The prediction was first reported in 1993 [10]; it is interesting to note that this was just two years after the seminal finding on carbon nanotubes. In the theoretically proposed structures, the coiling arose as a consequence of periodic insertion of topological defects into a perfect graphitic cylinder. Figure 3.15 presents three different kinds of proposed structures [10], in which the pentagons and heptagons inserted are marked by black and shadow, respectively. It should be noted that in the proposed structures, topological defects are not "defects" but essential building blocks for realizing the atomic coiling network. Furthermore, the presence of non-hexagonal rings gives a physico-chemical impact on carbon nanocoils; it was numerically found that local change in the atomic bonding around the non-hexagonal rings leads to an enhancement of molecular hydrogen absorption on the outer surface [87]. The enhanced hydrogen absorption on the body surface indicates the possibility of developing a new class of hydrogen storage devices based on carbon nanocoils and/or other defective sp^2 layered materials.

3.6.2 Atomistic Modeling

A simple atomistic modelling of carbon nanocoils was suggested in [88]. The modelling is based on insertion of heptagons and pentagons in a periodic manner into a hexagonal carbon network. First let us suppose a piece of straight carbon nanotube as depicted in Fig. 3.16a. Next, a pair of pentagons is incorporated onto one side of the piece (at the position colored in blue), and a pair of heptagons onto the other side (red). After relaxing the defective tube segment, we will see that it is bent around the non-hexagonal rings, through which the defect-induced strain energy is relieved [10,
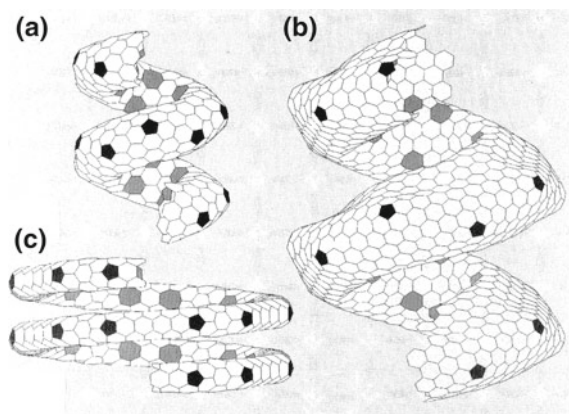
Fig. 3.15 Various atomic models of carbon coils with the lowest cohesive energy per atom. Pentagons and heptagons (shaded) appear in the outer and inner ridge lines, respectively, amid a background of the hexagonal lattice. Reprinted with permission from [10]
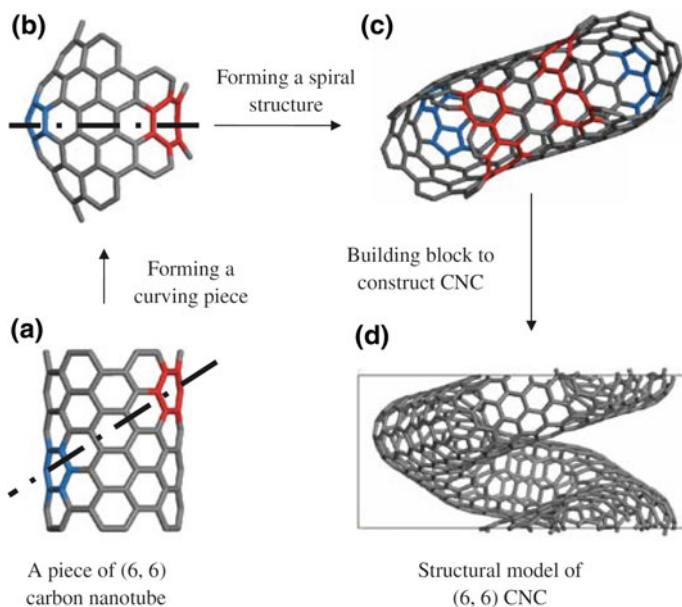

Fig. 3.16 Procedures of constructing a carbon nanocoil of a (6,6) type from pieces of a (6,6) carbon nanotube. Reprinted from [88]

89]. Similarly to previous arguments, pentagons generate positive curvature leading to a local cone shape, while heptagons generate negative curvature leading to a local saddle shape. The close relation between the defect position and the local change in the surface curvature is illustrated in Fig. 3.16b.

To obtain a spiral structure, we have only to connect the many building blocks already prepared one by one with a certain twisting angle. Figure 3.16c demonstrates a joint of two segments; repeating the connecting procedure, we finally obtain a seamless nanocoil as demonstrated in Fig. 3.16d. By changing the tube length at the two ends of the building block segment, or by varying the nanotube diameter, we can control coil diameter, coil pitch, and tubular diameter of a carbon nanocoil.

3.6.3 Experimental Realization

It may be surprising that experimental fabrication of carbon nanocoils has a relatively short story. The first electron microscopy observation of carbon nanocoils was reported in 1994 [90], serving as the pathfinder for the subsequent efforts both of high-quality production and of physical property investigation in carbon nanocoils. In the seminal work [90], catalytic decomposition of C_2H_2 worked successfully to synthesize carbon nanocoils with 30 nm in pitch and 18 nm in tubular diameter. Electron diffraction method was used to reveal the multiwalled, hollow, and polygonized structure, indicating that the nanocoils consisted of short straight segments. These structural features experimentally confirmed are consistent with the theoretical prediction that the introduction of pentagon-heptagon pairs at regular distances in a straight carbon nanotube results in the coiling morphology [89].

Since the first synthesis, many researchers have tried to make up these materials. Production of carbon nanocoils by chemical vapor deposition, laser evaporation, and opposed flow flame combustion method has been reported to date [5]. In addition to the "multi"-walled nanocoils with tubular diameters of several tens nanometers or more [91], indirect evidence of ultrathin "single"-walled carbon nanocoils (with both tubular diameter and pitch length down to 1 nm) was achieved by electron microscopy [92].

Among many syntheses so far, the triple-walled carbon nanocoil may be the thinnest one of which the direct microscopic image was obtained as a proof [93]. Figure 3.17 shows the image of the triple-walled nanocoil, having the fiber diameter less than 5 nm. It was synthesized by chemical vapor deposition under the following conditions: reaction temperature is 700 °C, the ratio of the source gas (acetylene, C_2H_2) to the dilution gas (nitrogen, N_2) is 0.01, and the gas pressure to be 0.67 kPa. A low C_2H_2 gas flow rate and a low partial gas pressure were important in reducing the fiber diameter.

3.6.4 Theoretical Prediction

For general twisted nanomaterials, geometric torsion is thought to result in significant impact on the coherent transport [94–97] and spin–orbit coupling [98, 99] of electrons migrating over the system. Namely, quantum transport through a nanoscale material

Fig. 3.17 Electron microscope image of a triple-walled carbon nanocoil. Reprinted with permission from [93]
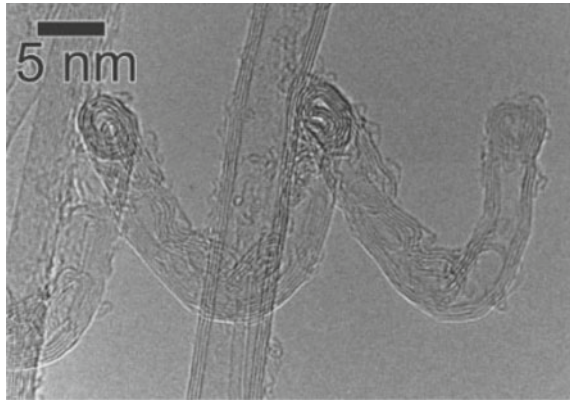
with torsion will be essentially different from that in a curved nanomaterial with no torsion. This is because geometric torsion of the host material generates an additional quantum potential that affects the quantum motion of carriers in the system. It is thus interesting whether such torsion effect is feasible in the quantum nature of carbon nanocoils; this remains an open question, especially from an experimental viewpoint, mainly because of the difficulty in synthesizing few-walled carbon nanocoils with fine crystalline structure.

Numerical efforts have also been underway to unveil the curvature (and/or topology) effect on the quantum transport in carbon nanocoils. For instance, tight-binding simulations have shown that the quantum conductance is quantized due to the translational symmetry in the coiled direction [100]. Yet the conductance behaviors differ greatly from those of pristine metallic carbon nanotubes; instead, it looks similar to those of carbon nanotube superlattices, as a manifestation of the periodic insertion of topological defects.

The thermal properties of carbon nanocoils are also an interesting subject. Nonequilibrium molecular dynamics simulations have been used to reveal that the thermal conductivity in carbon nanocoils is reduced up to 70% compared with that of the corresponding straight single-walled carbon nanotubes [101]. The extreme reduction is due to the phonon scattering by coupled defects and folding. Shortly afterward, phonon thermal transport in carbon nanocoils has been studied in detail [102]. The three-phonon Umklapp scattering rates and the associated phonon relaxation were considered in a wide temperature range, and a certain reduction in the thermal conductivity of carbon nanocoils was numerically detected as well.

As a final remark, it warrants comment on a recent finding on the quantum transport of a helicoidal graphene nanoribbon [103]. In this geometry, the twist of the nanoribbon plays the role of an effective transverse electric field in graphene. Surprisingly, this effective electric field turned out to have a different sign for the two isospin states; here, isospin is defined with regard to the two components of a Dirac spinor. As a result, this electric field reverses polarity when the isospin is changed, leading to a separation of the isospin states of the carriers on the opposing rims of the
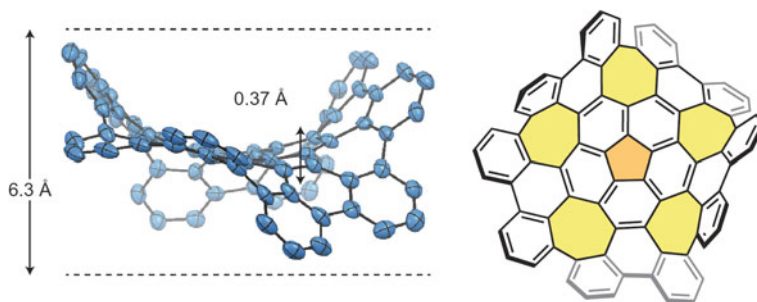
Fig. 3.18 Atomic structural model of a warped nanographene. All of the atoms shown in the image are carbons; hydrogen atoms on the perimeter are omitted for clarity. Reprinted with permission from [104]

nanoribbon. From the experimental feasibility, the isospin transitions are expected with the emission or absorption of microwave radiation which could be adjusted to be in the THz region.

3.7 State-of-the-Art Curved sp^2 Nanocarbons

3.7.1 Nano-"Pringles"

The final section covers several exotic sp^2 nanocarbons that were fabricated/predicted in the last few years. The first to be noted is the so-called nano-"Pringle" [104], i.e., a piece of warped nanographene comprising 80 carbon atoms joined together in a network of 26 rings. Figure 3.18 shows the atomic model of a nano-Pringle. Key to the formation of the grossly warped structure is the addition of five heptagons into the hexagonal lattice. Nano-Pringles turned out to show high solubility in common organic solvents and a widened energy gap between the highest occupied molecular orbital (HOMO) and the lowest unoccupied molecular orbital (LUMO) [104].

Interestingly, this unique structure was found to have physical and chemical properties distinct from other all-carbon families. For instance, the first-principles calculations revealed that the introduction of topological defects significantly changes the optical absorption spectra of nano-Pringles [105, 106]. In particular, the interaction between the topological defects was found to enhance the excitonic effect due to the lattice symmetry breaking, thereby generating the extra peaks at the lower photon energy side of the main peak.

From chemical perspective, the gas adsorption ability of nano-Pringles has drawn much attention recently. A series of numerical work has unveiled the adsorption property of small molecules, such as O_2, CO, and SO_2, on the nano-Pringles surface. For instance, adsorption of SO_2 turned out to induce charge transfer, indicating
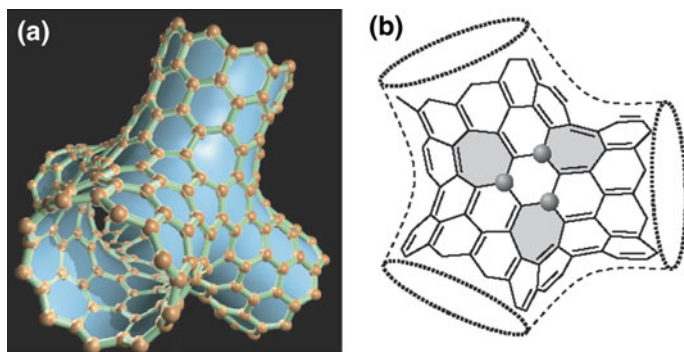
Fig. 3.19 a Nano-Tetrapod structure made of sp^2 carbon bondings. It is a junction of four (9, 0) nanotubes with a zigzag edge. **b** Chemical bonding near the core of the tetrapod. Trivalent carbon radicals are emphasized by gray spheres. Reprinted with permission from [109]

that the nano-Pringles can be used as an SO_2 sensor [107]. In addition, chemical adsorption of O_2 causes modulation in the HOMO-LUMO gap, implying the potential utility in optoelectronics [107]. Another salient feature of the nano-Pringles is the potential utility as the CO chemical sensors, for which the pristine graphene is not appropriate. Numerical simulation uncovered that the electronic conductivity of nano-Pringles increases with the CO concentration [108].

3.7.2 Nano- "Tetrapod"

Figure 3.19 displays the second remarkable example of exotic nanocarbons, so to say, a nano-"Tetrapod" [109]. This three-dimensional open structure is composed of a carbon network of hexagons and heptagons only. As found in Fig. 3.19, four cut-off pieces of carbon nanotubes with (9, 0) chirality are glued via several heptagons, forming a quadruped nanocarbon material. The tetrapod may serve as a building block of a nanostructured carbon foam [110].

One of the most striking features is that the nano-Tetrapod carries a net magnetic moment in the ground state. The origin of magnetism in the nano-Tetrapod is the presence of four unpaired spins in the electronic ground state. Accordingly, the ground state of the nano-Tetrapod is different either from the spin-polarized states at the zigzag edge or dangling-bond states, in which the spin polarization is attributed to the presence of under-coordinated carbon atoms. Instead, the magnetic behavior of the nano-Tetrapods stems from the trivalent carbon radicals introduced at the center of the quadruple structure. The radicals are sterically stabilized within the aromatic system of the otherwise tetravalent carbon atoms. The conclusion that unpaired spins may be introduced by carbon radicals, not only by under-coordinated carbon atoms,
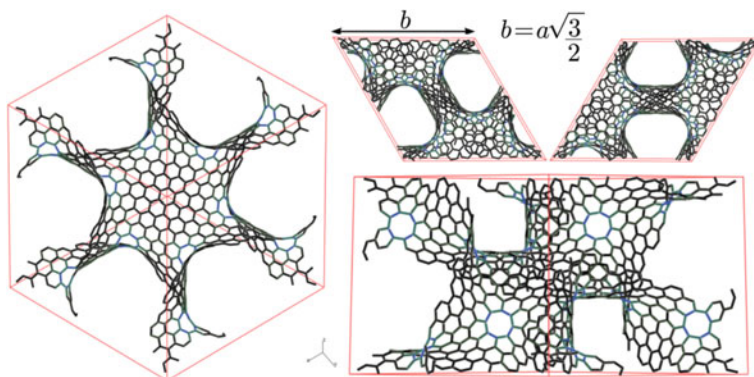
Fig. 3.20 Atomic structure of the gyroidal Schwarzite: the [111] orientation (left panel), the [100] and [010] orientation (top right panels), and the [110] orientation (bottom right panel). The arrow labeled by b indicates the lattice parameter. Reprinted with permission from [114]

will open a new avenue to design other graphitic structures with negative surface curvature.

3.7.3 Nano-"Schwarzite"

The last example of exotic sp^2 nanocarbons is carbon Schwarzite. It has been known as a negative-curvature analogue of the fullerenes since the early 1990s [111–113]. Figure 3.20 illustrates the atomic structure of a carbon Schwarzite with gyroidal type [114], in which non-hexagonal carbon rings stabilize the curved structure. Schwarzites are distinguished from the well-known sp^2 nanocarbon with 0D, 1D or 2D, by their hyperbolic geometry. Thus, such new type of geometry is expected to result in novel and fascinating properties.

In mathematics, the negative curvature surfaces of interest are called infinite periodic minimal surfaces, first studied in detail by the mathematician H. A. Schwarz in the late 19th century [115]. He pointed out that it is not possible to construct an infinite surface with a constant negative Gaussian curvature; instead, he found that patches of varying negative Gaussian curvature could be smoothly joined to provide an infinite surface with zero mean curvature, which is periodic in 3D space. Five different types of minimal surfaces were known by 1880 [116]; afterword, more than 50 types of distinct minimal surfaces have been discovered [117].

In the community of physics and materials science, Schwarzite structures have received increasing attention due to the interest in finding a graphene foam [118]. A number of periodic porous carbon structures similar to Schwarzite structures have been experimentally produced using, for example, templated synthesis [119] and liquid exfoliation techniques [120]. The enhanced control in the fabrication of

Schwarzite structures will open the way for versatile applications; hydrogen storage systems [121] and electrolyte diffusion [122] are only a few to mention. Quite recently, Schwarzite structures have been fabricated along the wall of zeolite pores; it was demonstrated that La ions embedded in zeolite pores facilitate the carbonization of ethylene or acetylene, enabling the selective formation of Schwarzite structures inside the zeolite template [123].

One interesting subject in view of quantum physics is the possible presence of pseudo-relativistic massless particles (Dirac fermions) in Schwarzite structures. The density functional calculations have revealed that a linear band crossing merging in a point for a large gyroidal Schwarzite structure [114]. Such a gapless linear energy dispersion in low-dimensional nanocarbons had a tremendous impact on conventional condensed-matter physics by imposing relativistic physics in the electronic properties of these nanosystems. Indeed, the electrons in graphene (2D) and carbon nanotubes (1D) behave like Dirac fermions as described by the crossing of linearly dispersive electronic bands, also called the Dirac cone. In this context, Schwarzites may be a remarkable playground to investigate relativistic physics of these exotic fermions, whereas their essential properties with respect to structural stability, mechanical, and electronic aspects should be largely investigated [124, 125].

3.8 Perspective

The synthesis or discovery of new materials, for example, fullerenes (1996 Nobel Prize in Chemistry), nanotubes, and graphene (2010 Nobel Prize in Physics) has been hitherto done on the basis of (1) knowledge (literature), (2) experience, and (3) intuition so far. These factors are still important, but it is wondered that we have failed to find the other fascinating materials close to them thus synthesized/discovered previously. In addition, it will take an unexpected time to discover the next new fascinating materials, because of "serendipity" based on (2) and (3) as shown in top (a) of Fig. 3.21.

Is it impossible that we can synthesize/discover new novel materials beyond "serendipity"? One possible way is to combine modern geometry with materials science. It is well known historically that Mathematics has been extensively used as a good tool in Physics and Chemistry (for example, differential and integral, point group, vector and tensor, etc.), but we have not seriously considered the correlation between geometric/topological quantity and physical/chemical quantity (properties) up to now, because there has been a large gap between mathematical simple model (point and line) and real materials (different atoms and different interactions between them).

As introduced in this chapter, geometry/topology can provide not only new forms but also new properties of nanocarbon materials. If geometric/topological quantity is correlated with physical/chemical quantity (properties), we can add new index "mathematics" to materials world consisting of two indexes "physics and chemistry" as shown in bottom (b) of Fig. 3.21. Thus we can synthesize/discover new
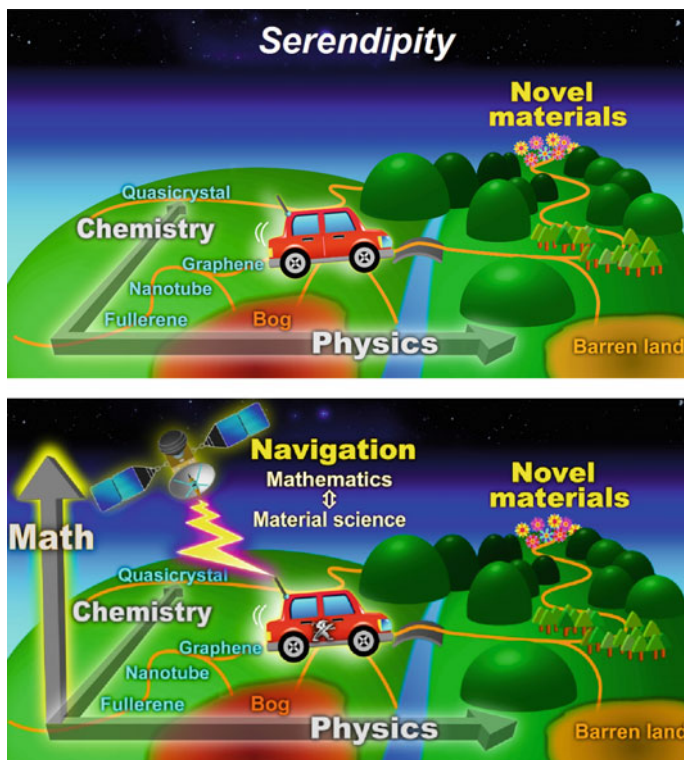
Fig. 3.21 Paradigm shift in materials science using Mathematics. Top: Conventional ways to discover novel materials. Bottom: Mathematics-navigated ways to discover novel materials

materials beyond "serendipity". More recently, materials informatics [combination of AI (artificial intelligence) with data-base of materials] has been focused from a viewpoint of materials development. It is a concern that they can find the optimal solution promptly for a given material, but may hardly find new or unexpected solution as far as using the data-base.

References

1. S. Gupta, A. Saxena, J. Appl. Phys. **109**, 074316 (2011)
2. S. Gupta, A. Saxena, MRS Bull. **39**, 265–279 (2014)
3. X. Chen, G. Wu, Y. Jiang, Y. Wang, X. Chen, Analyst **136**, 4631–4640 (2011)
4. S. Iijima, Nature **354**, 56–58 (1991)

5. H. Shima, M. Sato, *Elastic and Plastic Deformation of Carbon Nanotubes* (Pan Stanford Publishing, Singapore, 2013)
6. K.S. Novoselov, A.K. Geim, S.V. Morozov, D. Jiang, Y. Zhang, S.V. Dubonos, I.V. Grigorieva, A.A. Firsov, Science **306**, 666–669 (2004)
7. M.T. Lusk, L.D. Carr, Phys. Rev. Lett. **100**, 175503 (2008)
8. H. Shima, *Functional Analysis for Physics and Engineering: An Introduction* (CRC Press, 2016)
9. J. Onoe, T. Nakayama, M. Aono, T. Hara, Appl. Phys. Lett. **82**, 595–597 (2003)
10. S. Ihara, S. Itoh, Phys. Rev. B **48**, 5643–5648 (1993)
11. A.L. Mackay, H. Terrones, Nature **352**, 762 (1991)
12. H. Terrones, A.L. Mackay, Carbon **30**, 1251–1260 (1992)
13. H. Terrones, M. Terrones, New J. Phys. **5**, 126 (2003)
14. A. Cortijo, M.A.H. Vozmediano, Nucl. Phys. B **763**, 293–308 (2007)
15. O.V. Yazyev, S.G. Louie, Phys. Rev. B **81**, 195420 (2010)
16. M.V. Diudea, Phys. Chem. Chem. Phys. **7**, 3626–3633 (2005)
17. T. Zhang, X. Li, H. Gao, Ext. Mech. Lett. **1**, 3–8 (2014)
18. J.M. Carlsson, M. Scheffler, Phys. Rev. Lett. **96**, 046806 (2006)
19. J. Kang, J. Bang, B. Ryu, K.J. Chang, Phys. Rev. B **77**, 115453 (2008)
20. D.V. Kolesnikov, V.A. Osipov, JETP Lett. **87**, 419–422 (2008)
21. Y. Noda, S. Ono, K. Ohno, Phys. Chem. Chem. Phys. **16**, 7102–7107 (2014)
22. O.V. Yazyev, S.G. Louie, Nat. Mater. **9**, 806–809 (2010)
23. A.V. Zhukov, R. Bouffanais, N.N. Konobeeva, M.B. Belonenko, JETP Lett. **97**, 400–403 (2013)
24. T. Choudhari, N. Deo, EPL (Europhys. Lett.) **108**, 57006 (2014)
25. Y. Zhu, S. Murali, M.D. Stoller, K.J. Ganesh, W. Cai, P.J. Ferreira, A. Pirkle, R.M. Wallace, K.A. Cy-chosz, M. Thommes, D. Su, E.A. Stach, R.S. Ruoff, Science **332**, 1537–1541 (2011)
26. D. Odkhuu, D.H. Jung, H. Lee, S.S. Han, S.H. Choi, R.S. Ruoff, N. Park, Carbon **66**, 39–47 (2014)
27. S. Zhang, J. Zhou, Q. Wang, X. Chen, Y. Kawazoe, P. Jena, Proc. Natl. Acad. Sci. USA **112**, 2372–2377 (2015)
28. M. Terrones, F. Banhart, N. Grobert, J.C. Charlier, H. Terrones, P.M. Ajayan, Phys. Rev. Lett. **89**, 075505 (2002)
29. M. Menon, A.N. Andriotis, D. Sri-vastava, I. Ponomareva, L.A. Chernozatonskii, Phys. Rev. Lett. **91**, 145501 (2003)
30. M. Yoon, S. Han, G. Kim, S.B. Lee, S. Berber, E. Osawa, J. Ihm, M. Terrones, F. Banhart, J.C. Charlier, N. Grobert, H. Terrones, P.M. Ajayan, D. Tománek, Phys. Rev. Lett. **92**, 075504 (2004)
31. B.I. Dunlap, Phys. Rev. B **46**, 1933–1936 (1992)
32. J. Zhang, D. Jiang, Compos. Sci. Technol. **71**, 466–470 (2011)
33. L. Liu, L. Zhang, J. Lua, Appl. Phys. Lett. **101**, 161907 (2012)
34. Y. Suda and H. Shima, Metal Powder Rep. **72**, 317–321 (2017). https://doi.org/10.1016/j.mprp.2016.06.005
35. J.W. Jang, C.E. Lee, S.C. Lyu, T.J. Lee, C.J. Lee, Appl. Phys. Lett. **84**, 2877–2879 (2004)
36. S. Shanmugam, A. Gedanken, J. Phys. Chem. B **110**, 2037–2044 (2006)
37. L. Gan, R. Lv, H. Du, B. Li, F. Kang, Carbon **47**, 1833–1840 (2009)
38. T.W. Ebbesen, Acc. Chem. Res. **31**, 558–566 (1998)
39. M. Terrones, ACS Nano **4**, 1775–1781 (2010)
40. Y. Saito, K. Hata, T. Murata, Jpn. J. Appl. Phys. **39**, L271–L272 (2000)
41. Y. Nishiura, M. Kotani, *Mathematical Challenges in a New Phase of Materials Science* (Springer, 2014)
42. J.R. Sanchez-Valencia, T. Dienel, O. Gröning, I. Shorubalko, A. Mueller, M. Jansen, K. Amsharov, P. Ruffieux, R. Fasel, Nature **512**, 61–64 (2014)
43. A.J. Stone, D.J. Wales, Chem. Phys. Lett. **128**, 501–503 (1986)

44. K.S. Novoselov, A.K. Geim, S.V. Morozov, D. Jiang, M.I. Katsnelson, I.V. Grigorieva, S.V. Dubonos, A.A. Firsov, Nature **438**, 197 (2005)
45. X. Peng, R. Ahuja, Nano Lett. **8**, 4464 (2008)
46. A.I. Podlivaev, L.A. Openov, Phys. Lett. A **379**, 1757 (2015)
47. J. Ma, D. Alfè, A. Michaelides, E. Wang, Phys. Rev. B **80**, 033407 (2009)
48. K. Balasubramanian, M. Burghard, Small **1**, 180–192 (2005)
49. J. Zhao, H. Park, J. Han, J.P. Lu, J. Phys. Chem. B **108**, 4227 (2004)
50. M. Ouyang, J.L. Huang, C.L. Cheung, C.M. Lieber, Science **291**, 97–100 (2001)
51. A. Hashimoto, K. Suenaga, A. Gloter, K. Urita, S. Iijima, Nature **430**, 870–873 (2004)
52. M. Ishigami, H.J. Choi, S. Aloni, S.G. Louie, M.L. Cohen, A. Zettl, Phys. Rev. Lett. **93**, 196803 (2004)
53. K. Suenaga, H. Wakabayashi, M. Koshino, Y. Sato, K. Urita, S. Iijima, Nat. Nanotechnol. **2**, 358–360 (2007)
54. M. Yudasaka, H. Kataura, T. Ichihashi, L.C. Qin, S. Kar, S. Iijima, Nano Lett. **1**, 487–489 (2001)
55. J.C. Meyer, C. Kisielowski, R. Erni, M.D. Rossell, M.F. Crommie, A. Zettl, Nano Lett. **8**, 3582–3586 (2008)
56. S.T. Skowron, V.O. Koroteev, M. Baldoni, S. Lopatin, A. Zurutuza, A. Chuvilin, E. Besley, Carbon **105**, 176–182 (2016)
57. B.I. Yakobson, Appl. Phys. Lett. **72**, 918–920 (1998)
58. M.B. Nardelli, B.I. Yakobson, J. Bernholc, Phys. Rev. B **57**, R4277–R4280 (1998)
59. H. Mori, S. Ogata, J. Li, S. Akita, Y. Nakayama, Phys. Rev. B **74**, 165418 (2006)
60. Y. Nakayama, Jpn. J. Appl. Phys. **46**, 5005–5014 (2007)
61. T. Zhang, X. Li, H. Gao, J. Mech. Phys. Solid. **67**, 2–13 (2014)
62. H. Masuda, J. Onoe, H. Yasuda, Carbon **81**, 842–846 (2015)
63. H. Masuda, H. Yasuda, J. Onoe, Carbon **96**, 316–319 (2016)
64. H. Ueno, S. Osawa, E. Osawa, K. Takeuchi, Fuller. Sci. Technol. **6**, 319–338 (1998)
65. S. Ono, Y. Toda, J. Onoe, Phys. Rev. B **90**, 155435 (2014)
66. H. Shima, Geometry-property relation in corrugated nanocarbon cylinders, in *Modeling of Carbon Nanotubes, Graphene and Their Composites* (Springer, 2014)
67. Y. Toda, S. Ryuzaki, J. Onoe, Appl. Phys. Lett. **92**, 094102 (2008)
68. J. Onoe, A. Takashima, Y. Toda, Appl. Phys. Lett. **97**, 241911 (2010)
69. J. Onoe, A. Takashima, S. Ono, H. Shima, T. Nishii, J. Phys.: Condens. Matter **24**, 175405 (2012)
70. J. Voit, Rep. Prog. Phys. **57**, 977 (1994)
71. H. Ishii, H. Kataura, H. Shiozawa, H. Yoshioka, H. Otsubo, Y. Takayama, T. Miyahara, S. Suzuki, Y. Achiba, M. Nakatake, T. Narimura, M. Higashiguchi, K. Shimada, H. Namatame, M. Taniguchi, Nature **426**, 540–544 (2003)
72. H. Yoshioka, H. Shima, Y. Noda, S. Ono, K. Ohno, Phys. Rev. B **93**, 165431 (2016)
73. J. Onoe, T. Ito, H. Shima, H. Yoshioka, S. Kimura, EPL (Europhys. Lett.) **98**, 27001 (2012)
74. Y. Noda, S. Ono, K. Ohno, J. Phys. Chem. A **119**, 3048–3055 (2015)
75. T.A. Beu, J. Onoe, A. Hida, Phys. Rev. B **72**, 155416 (2005)
76. R.C.T. da Costa, Phys. Rev. A **23**, 1982 (1981)
77. H. Shima, H. Yoshioka, J. Onoe, Phys. Rev. B **79**, 201401 (2009)
78. M. Kociak, A.Y. Kasumov, S. Guéron, B. Reulet, I.I. Khodos, Y.B. Gorbatov, V.T. Volkov, L. Vaccarini, H. Bouchiat, Phys. Rev. Lett. **86**, 2416 (2001)
79. J.Y. Park, S. Rosenblatt, Y. Yaish, V. Sazonova, H. Üstünel, S. Braig, T.A. Arias, P.W. Brouwer, P.L. McEuen, Nano Lett. **4**, 517 (2004)
80. P. Zhou, K.-A. Wang, P.C. Eklund, G. Dresselhaus, M.S. Dresselhaus, Phys. Rev. B **48**, 8412–8417 (1993)
81. T. Hertel, R. Fasel, G. Moos, Appl. Phys. A **75**, 449 (2002)
82. I. Chatzakis, Appl. Phys. Lett. **103**, 043110 (2013)
83. S. Ono, Y. Toda, J. Onoe, Phys. Rev. B **90**, 155435 (2014)

84. H. Shima, Y. Suda, Mechanics of helical carbon nanomaterials, in *Advanced Computational Nanomechanics* (Wiley, 2015)
85. X. Chen, S. Zhang, D.A. Dikin, W. Ding, R.S. Ruoff, L. Pan, Y. Nakayama, Nano Lett. **3**, 1299–1304 (2003)
86. A. Volodin, D. Buntinx, M. Ahlskog, A. Fonseca, J.B. Nagy, C.V. Haesendonck, Nano Lett. **4**, 1775–1779 (2004)
87. V. Gayathri, N.R. Devi, R. Geetha, Int. J. Hydro. Energ. **35**, 1313–1320 (2010)
88. L.Z. Liu, H.L. Gao, J.J. Zhao, J.P. Lu, Nanoscale Res. Lett. **5**, 478–483 (2010)
89. S. Ihara, S. Itoh, J. Kitakami, Phys. Rev. B **47**, 12908–12911 (1993)
90. V. Ivanov, J.B. Nagy, Ph Lambin, A. Lucas, X.B. Zhang, X.F. Zhang, D. Bemaerts, G.V. Tendeloo, S. Amelinckx, J. van Landuyt, Chem. Phys. Lett. **223**, 329–335 (1994)
91. K.T. Lau, Composites B **37**, 437–448 (2006)
92. L.P. Biró, S.D. Lazarescu, P.A. Thiry, A. Fonseca, J.B. Nagy, A.A. Lucas, P. Lambin, Europhys. Lett. **50**, 494–500 (2000)
93. S.L. Lim, Y. Suda, K. Takimoto, Y. Ishii, K. Maruyama, H. Tanoue, H. Takikawa, H. Ue, K. Shimizu, Y. Umeda, Jpn. J. Appl. Phys. **52**, 11NL04 (2013)
94. J. Goldstone, R.L. Jaffe, Phys. Rev. B **45**, 14100 (1992)
95. H. Taira, H. Shima, J. Phys. Condens. Matt. **22**, 075301 (2010)
96. G. Cuoghi, A. Bertoni, A. Sacchetti, Phys. Rev. B **83**, 245439 (2011)
97. G.H. Liang, Y.L. Wang, L. Du, H. Jiang, G.Z. Kang, H.S. Zong, Physica E **83**, 246–255 (2016)
98. C. Ortix, Phys. Rev. B **91**, 245412 (2015)
99. P. Gentile, M. Cuoco, C. Ortix, Phys. Rev. Lett. **115**, 256801 (2015)
100. W. Lu, Sci. Technol. Adv. Mater. **6**, 809–813 (2005)
101. J. Zhao, J. Wu, J.W. Jiang, L. Lu, Z. Zhang, T. Rabczuk, Appl. Phys. Lett. **103**, 233511 (2013)
102. Z.P. Popović, M. Damnjanović, I. Milošević, Carbon **77**, 281–288 (2014)
103. V. Atanasov, A. Saxena, Phys. Rev. B **92**, 035440 (2015)
104. K. Kawasumi, Q. Zhang, Y. Segawa, L.T. Scott, K. Itami, Nat. Chem. **5**, 739 (2013)
105. Y. Noguchi, O. Sugino, J. Chem. Phys. **142**, 064313 (2015)
106. X. Wang, S. Yu, Z. Lou, Q. Zeng, M. Yang, Phys. Chem. Chem. Phys. **17**, 17864–17871 (2015)
107. Y. Dai, Z. Li, J. Yang, Carbon **100**, 428–434 (2016)
108. S. Jameh-Bozorghi, H. Soleymanabadi, Phys. Lett. A **381**, 646–651 (2017)
109. N. Park, M. Yoon, S. Berber, J. Ihm, E. Osawa, David Tomanek, Phys. Rev. Lett. **91**, 237204 (2003)
110. A.V. Rode, E.G. Gamaly, B. Lu-ther-Davies, Appl. Phys. A **70**, 135 (2000)
111. A.L. Mackay, H. Terrones, Nature **352**, 762 (1991)
112. T. Lenosky, X. Gonze, M. Teter, E. Vert, Nature **355**, 333 (1992)
113. M. O'Keeffe, G.B. Adams, O.F. Sankey, Phys. Rev. Lett. **68**, 2325 (1992)
114. A. Lherbier, H. Terrones, J.-C. Charlier, Phys. Rev. B **90**, 125434 (2014)
115. H.A. Schwarz, *Gesammelte Mathematische Abhandlungen* (Springer, 1890)
116. E.R. Neovius, *Bestimmung Zweier Spezieller Periodische Minimalflächen* (J. C. Frenkel & Sohn, Hel-sinki, 1883)
117. W. Fischer, E. Koch, Acta Cryst. A **45**, 166,169, 485, 558, 726 (1989)
118. Y. Wu, N. Yi, L. Huang, T. Zhang, S. Fang, H. Chang, N. Li, J. Oh, J.A. Lee, M. Kozlov, A.C. Chipara, H. Terrones, P. Xiao, G. Long, Y. Huang, F. Zhang, L. Zhang, X. Lepró, C. Haines, M.D. Lima, N.P. Lopez, L.P. Rajukumar, A.L. Elias, S. Feng, S.J. Kim, N.T. Narayanan, P.M. Ajayan, M. Terrones, A. Aliev, P. Chu, Z. Zhang, R.H. Baughman, Y. Chen, Nat. Commun. **6**, 6141 (2015)
119. H. Nishihara, T. Kyotani, Adv. Mater. **24**, 4473–4498 (2012)
120. J.G. Werner, T.N. Hoheisel, U. Wiesner, ACS Nano **8**, 731–743 (2014)
121. P. Kowalczyk, R. Hołyst, M. Terro-nes, H. Terrones, Phys. Chem. Chem. Phys. **9**, 1786–1792 (2007)
122. A. Nicolaï, J. Monti, C. Daniels, V. Meunier, J. Phys. Chem. C **199**, 2896–2903 (2015)

123. K. Kim, T. Lee, Y. Kwon, Y. Seo, J. Song, J.K. Park, H. Lee, J.Y. Park, H. Ihee, S.J. Cho, R. Ryoo, Nature **535**, 131–135 (2016)
124. J.R. Owens, C. Daniels, A. Nicolaï, H. Terrones, V. Meunier, Carbon **96**, 998–1007 (2016)
125. D.C. Miller, M. Terrones, H. Terrones, Carbon **96**, 1191–1199 (2016)